Mechanical Spectroscopy Investigation of Point Defect-Driven Phenomena in a Cr Martensitic Steel

Alessandra Fava, Roberto Montanari * and Alessandra Varone

Department of Industrial Engineering, University of Rome "Tor Vergata", 00133 Rome, Italy; alessandra.fava@uniroma2.it (A.F.); alessandra.varone@uniroma2.it (A.V.)

* Correspondence: roberto.montanari@uniroma2.it; Tel.: +39-06-7259-7182

Abstract: The paper presents and discusses results of mechanical spectroscopy (MS) tests carried out on a Cr martensitic steel. The study regards the following topics: (i) embrittlement induced by Cr segregation; (ii) interaction of hydrogen with C–Cr associates; (iii) nucleation of Cr carbides. The MS technique permitted characterising of the specific role played by point defects in the investigated phenomena: (i) Cr segregation depends on C–Cr associates distribution in as-quenched material, in particular, a slow cooling rate (~150 K/min) from austenitic field involves an unstable distribution, which leads to Cr concentration fluctuations after tempering at 973 K; (ii) hydrogen interacts with C–Cr associates, and the phenomenon hinders hydrogen attack (HA) because hydrogen atoms bound by C–Cr associates are not able to diffuse towards grain boundaries and dislocation where CH_4 bubbles may nucleate, grow, and merge to form the typical HA cracks; (iii) C–Cr associates take part in the nucleation mechanism of Cr_7C_3 carbides, and specifically these carbides form by the aggregation of C–Cr associates with 1 Cr atom.

Keywords: mechanical spectroscopy; Cr martensitic steel; point defects

1. Introduction

The role played by point defects is of the utmost relevance in several phenomena occurring in pure metals and alloys. Point defects (vacancies, interstitials, substitutional atoms, etc.) alter the elastic constants of a solid, strongly affect diffusion and ordering, and are relevant for irradiation, cold work, and recovery; thus, they have received a lot of attention since the 1960s (see, for example refs. [1,2]). Vacancies and self-interstitials play an important role also in metal melting [3–5] and, recently, some works demonstrated that a remarkable increase of self-interstitials takes place in a temperature range of about 10 K before melting, weakens interatomic bonds, and favours the final avalanche of vacancies, leading to the solid–liquid transformation [6–11].

Investigations by means of conventional techniques (hardness tests, resistivity measurements, X-ray diffraction, and dilatometry) give information only on the presence and annihilation of point defects. A much more complete description, including concentration, mobility, and symmetry, is obtained through mechanical spectroscopy (MS). The theory of point defect relaxations and the applications of the technique are described in the classical book of Nowick and Berry [12].

This paper presents and discusses results obtained through MS tests on a Cr martensitic steel. The experimental approach and analysis method can be extended to all the steels of this type, materials of great interest for many industrial applications. In particular, the focus of the study is on the following topics: (i) Cr segregation phenomena; (ii) interaction of hydrogen with C–Cr associates; (iii) nucleation of Cr carbides.

Cr martensitic steels are materials of great interest for structural applications in future nuclear fusion reactors, and a lot of work has been done to design and produce low activation steels with higher

resistance to swelling and embrittlement under irradiation. One of the authors has been involved in extensive experimental campaigns for investigating the microstructure of Cr martensitic steels with different Cr contents, and prepared under different conditions of quenching and tempering treatments. The scope was to understand how specific microstructural features affect swelling and brittle behaviour [13–25]. It was demonstrated that states of strain remain in non-irradiated steels after prolonged heat treatments, sufficient to anneal out dislocations and sub-boundaries, and their origin was attributed to the non-homogeneous Cr distribution in the matrix.

Different cooling rates from the austenitic field (1348 K) do not seem to have effects on the microstructure and mechanical properties of the steel, however, successive steps of tempering treatment determine different fracture modes. The present paper shows that such apparently anomalous behaviour depends on elementary structures of point defects (C–Cr associates).

Furthermore, the same structures affect both the hydrogen attack and the precipitation of Cr carbides.

2. Material and Methods

The nominal chemical composition of the investigated steel is reported in Table 1.

Table 1. Chemical composition of the investigated Cr martensitic steel (wt %).

C	Cr	Mo	Ni	Mn	Nb	V	Si	Al	N	P	Fe
0.17	10.50	0.50	0.85	0.60	0.20	0.20	0.25	0.32	0.05	0.003	0.005	to balance

MS experiments were carried out using bar-shaped samples (60 mm × 7 mm × 0.5 mm) excited by flexural vibrations and operating in conditions of resonance (frequencies in the range 150–400 Hz). The VRA 1604 apparatus (CANTIL Srl, Bologna, Italy) used in MS experiments has been described in detail in [26]. MS measurements are quite sensitive to experimental conditions, in particular, the heating rate and the strain amplitude, which should be taken strictly as constant. VRA 1604 allows for measurement of dynamic modulus and damping (Q^{-1}) with high precision and accuracy, characteristics of fundamental importance to perform the successive analyses.

The damping factor Q^{-1} was determined from the logarithmic decay δ of flexural vibrations:

$$Q^{-1} = \frac{\delta}{\pi} = \frac{1}{k\pi} \ln \frac{A_n}{A_{n+k}} \, , \tag{1}$$

A_n and A_{n+k} being the amplitude of the n-th and $n + k$-th vibration, respectively. The dynamic modulus E was calculated from the resonance frequency f:

$$E = \frac{48\pi^2 L^4 \rho}{m^4 h^2} f^2 \, , \tag{2}$$

with m being a constant depending on the specific sample geometry (for a reed $m = 1.875$), ρ the material density, and L and h the length and thickness of the sample, respectively. The heating rate was 2 K/min, while the strain amplitude was kept lower than 1×10^{-5}.

Scanning electron microscopy (SEM Hitachi S-2460N, Hitachi, Tokyo, Japan) observations have been carried out on the fracture surfaces of probes broken in Charpy tests and on carbides extracted from the metallic matrix. Extraction was carried out through an electrochemical method (solution of HCl (10%) in methanol, cathode of AISI 316 steel, operative temperature 300 K, tension 1.5 V, and current 0.5 A). The filtering was made using a membrane with pores of 0.1 μm. The extracted carbides were then examined by X-ray diffraction (Philips, Eindhoven, The Netherlands) and SEM observations with EDS microanalysis (Thermo Fisher Scientific, Madison, WI, USA). XRD spectra have been recorded using Mo-Kα radiation, in the 2θ range 5–20° by scanning with 2θ steps of 0.05° and a counting time of 5 s per step.

3. Results and Discussion

3.1. Q^{-1} Spectra Analysis

As shown by the examples in Figure 1, the Q^{-1} vs. temperature spectra of the Cr martensitic steel exhibit a complex scenario with more peaks of different position and intensity [27], depending on the quenching rate from austenitic field. Dynamic modulus *E*, normalised to the room temperature value E_0, exhibits slope changes in correspondence of the Q^{-1} peaks, indicating that they are relaxation peaks.
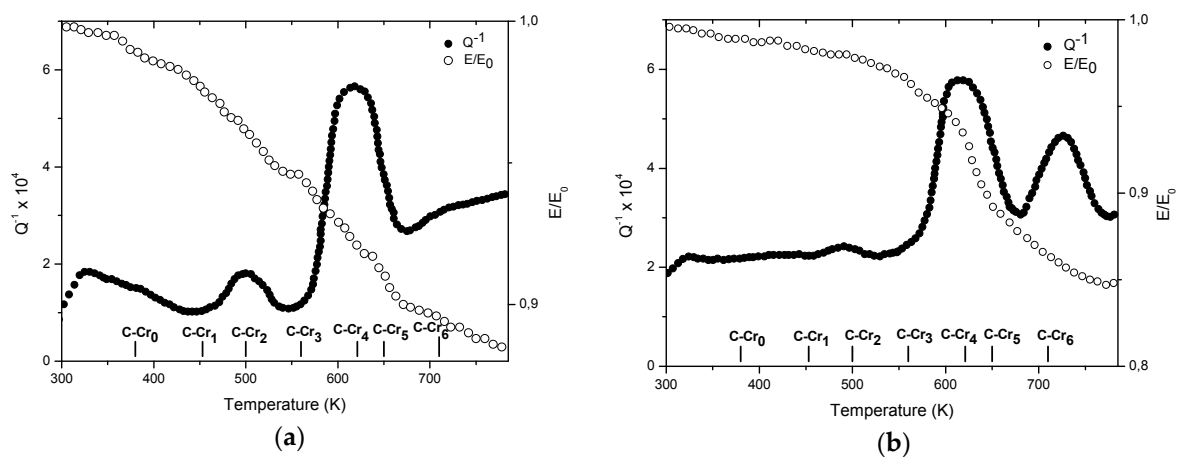
Figure 1. Q^{-1} and *E/Eo* curves of the Cr martensitic steel after quenching from the austenitic field (1348 K) with a cooling rate of 3600 K/min (**a**) and 150 K/min (**b**). The resonance frequency *f* = 250 Hz. Data of these materials where already published in ref. [27] but the present curves obtained through VRA 1604 are more pricise in particular in the initial part.

To understand the origin of the damping peaks, the interaction of C atoms in interstitial positions, with the atoms (Fe and Cr) forming the bcc lattice, has been considered. As shown in Figure 2, C atoms in solid solution are assumed to occupy the octahedral interstices in the bcc lattice of the steel.
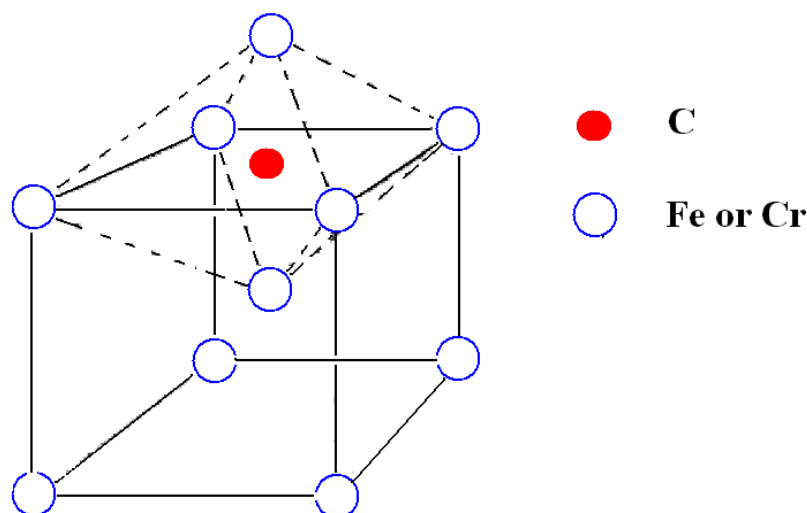
Figure 2. C atoms are allocated in the octahedral interstices of bcc lattice. The corners of the octahedron can be occupied by either Fe or Cr atoms, giving rise to seven possible C–Cr configurations.

In the Fe–C system, all the interstitial positions are energetically equivalent, and any inhomogeneity in C atoms distribution only depends on possible interactions with lattice defects, for instance, dislocations (Cottrell's atmospheres). If other alloying elements are present, they can substitute Fe atoms at the octahedron corners, giving rise to different configurations. In the Fe–Cr–C

system, typical of the investigated steel, the corners of each octahedron can be occupied by a number i of Cr atoms, varying from 0 to 6, thus 7 different C–Cr configurations may occur, each of them with a specific binding energy for the C atom.

Some theoretical models describing the effects of substitutional atoms on the Snoek peak have been developed, and a lot of data can be found in the handbook of Blanter et al. [28]. One of the first theories describing the effects of Cr atoms in the bcc Fe lattice was proposed by Tomilin et al. [29]. According to this model, $H_0 = 20$ kcal/mol is the activation energy when only Fe atoms are present at the corners of the octahedron, and a contribution $\Delta H = 3.1$ kcal/mol has to be added to H_0 for every Cr atom substituting a Fe atom. On this basis, the Q^{-1} curves consist of the overlapping of seven Snoek-type peaks corresponding to the aforesaid configurations. The activation energies and the positions of the peaks calculated for a resonance frequency of 250 Hz, typical of present experiments, are summarised in Table 2.

Table 2. Activation energies and peak positions of the seven $Q^{-1}{}_i$ peaks corresponding to octahedral configurations with a number of Cr atoms i varying from zero to six. (Resonance frequency f = 250 Hz.)

Number of Cr Atoms i	0	1	2	3	4	5	6
Activation energy (kcal/mol)	20.0	23.1	26.2	29.3	32.4	35.5	38.6
Peak position (K)	380	453	500	560	621	650	710

On these grounds, the Q^{-1} curves can be considered as the sum of seven contributions:

$$Q^{-1} = \sum_{i=0}^{6} Q^{-1}{}_i = \sum_{i=0}^{6} \Delta_i \frac{\omega\tau_i}{1+\omega^2\tau_i^2} = \sum_{i=0}^{6} \Delta_i sech\left[\left(\frac{H_0 + i\Delta H}{R}\right)\left(\frac{1}{T} - \frac{1}{T_i}\right)\right], \tag{3}$$

where R is the gas constant, $\omega = 2\pi f$, Δ_i the relaxation strength of peak $Q^{-1}{}_i$, proportional through a factor $\lambda \cong 50$ to the concentration C_i of C atoms in octahedral sites with i Cr atoms, T_i the peak temperature, and τ_i its relaxation time, given by

$$\tau_i = \tau_0 \exp -\left(\frac{H_0 + i\Delta H}{RT}\right), \tag{4}$$

with τ_0 being about 10^{-15} s.

The Tomilin's model assumes that, at the thermodynamic equilibrium, the number P_i of configurations with i atoms of Cr obeys a binomial distribution:

$$P_i = \frac{6!(1-N)^{6-i}N^i}{i!(6-i)!}, \tag{5}$$

where N is the Cr molar concentration. The concentration of C atoms in interstices with i Cr neighbours results in being

$$C_i = P_i\xi_0 / \left[\exp -\left(\frac{i\Delta H}{RT}\right) + (1 - \exp -(i\Delta H/RT))\xi_0\right] \tag{6}$$

where ξ_0 is the probability of occupation of interstices with $i = 0$.

Figure 3 shows the Q^{-1} curve calculated on the basis of Equation (3) for an alloy with the same Cr and C content of the examined steel, according to the assumptions of Tomilin's model expressed by Equations (5) and (6).

The comparison between the curves in Figure 1a,b and that in Figure 3 (re-drawn from ref. [27]) clearly shows that both the experimental curves differ from that predicted by the model. The experimental curves substantially exhibit peaks centred at the temperatures foreseen by the model and reported in Table 2, however, the intensities of the peaks (relaxation strengths Δ_i) do not correspond. This means that the distributions of C–Cr associates in both cases are not those of

thermodynamic equilibrium, and the different distributions depend on the cooling rate from the austenitic field.
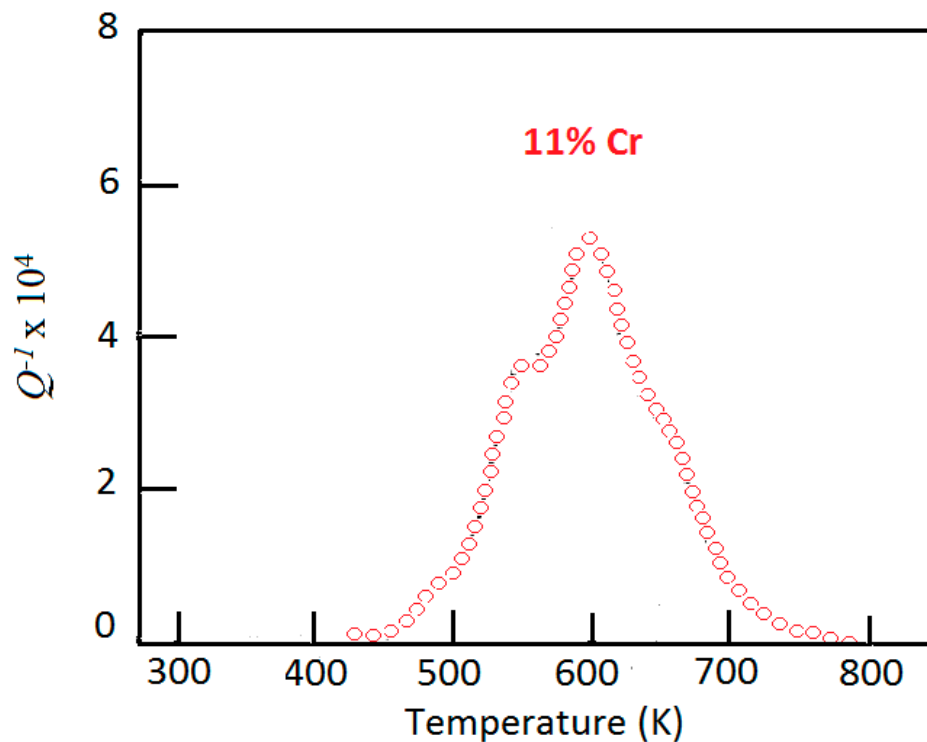
Figure 3. Q^{-1} curve for an alloy with the same Cr and C content of the examined steel, calculated on the basis of Equation (3), according to the assumptions of Tomilin's model. These data were already published in ref. [27], but the present curve obtained through VRA 1604 is more precise in particular in the initial part.

To analyse the Q^{-1} curves of the steel under different conditions of quenching, heat treatment etc., they have been fitted by considering the possible anelastic processes contributing to the damping. In addition to the relaxation peaks due to C–Cr associates, further contributions to the curves come from background and peaks connected to N relaxation processes.

The background is mainly due to the interactions of dislocations with interstitial atoms (C and N) and exhibits an increasing trend with temperature that can be described by an exponential function.

The damping contributions of N are, in fact, the same Q^{-1} peaks observed in Fe–Cr–N alloys by Ritchie and Rawlings [30]. Four peaks have been observed: the first and second peaks, attributed by these investigators to N/Cr–Cr interactions, have activation energies of 16.19 and 16.98 kcal/mol, respectively, and are centred for our resonance frequency (~250 Hz) at 324 K and 339 K. The third one, ascribed to Fe–N interactions, has an activation energy of 18.58 kcal/mol and is centred at 360 K. The fourth peak, due to N/Fe–Cr interactions, has an activation energy of 20.78 kcal/mol, and its temperature is 410 K.

In fact, Q^{-1} spectra are mainly affected by N contributions in the low temperature range, and by C contributions in the high temperature range.

The curve fitting of the experimental data is the sum of all the peaks due to C and N, and the background, therefore, it can be written as

$$Q^{-1} = \sum_{i=0}^{6} \Delta_i \sec h\left[\left(\frac{H_0 + i\Delta H}{R}\right)\left(\frac{1}{T} - \frac{1}{T_i}\right)\right] + \sum_{k=1}^{4} \Delta_k \sec h\left[\left(\frac{H_k}{R}\right)\left(\frac{1}{T} - \frac{1}{T_k}\right)\right] + A\exp\left(-\frac{T}{B}\right) + C, \tag{7}$$

where H_k and T_k are the activation energies and peak temperatures of N peaks, while A, B, and C are constants.

Since the background depends on microstructural features, such as dislocations and point defects, it is not the same in samples prepared in a different way, thus, the values of A, B, and C have to be determined for each single spectrum.

Once determined, the background curve, the activation energies (H_i and H_k), and the corresponding peak temperatures (T_i and T_k) of C and N peaks, are introduced into Equation (7), and the relaxation strengths Δ_i and Δ_k are suitably adjusted to find the best fitting curve.

Moreover, it has been assumed that the activation energy of each single relaxation process could be affected by small variations with respect that considered by the Tomilin's model, owing to a possible different environment surrounding the octahedra involved in the process, in particular, the number of Cr atoms present in the nearest atomic shells. Therefore, some shifts with respect to the temperatures T_i, reported in Table 2, have been considered to get the best fitting.

For example, Figure 4 displays the analysis of the Q^{-1} spectra in Figure 1. Table 3 reports the peak positions and relaxation strengths, Δ_i, used to calculate the different contributions which allow the best fit. The temperature of C–Cr$_4$ and C–Cr$_6$ peaks are a little shifted with respect to the values predicted by the Tomilin's model; the shifts correspond to variations of activation energies of about 1%.
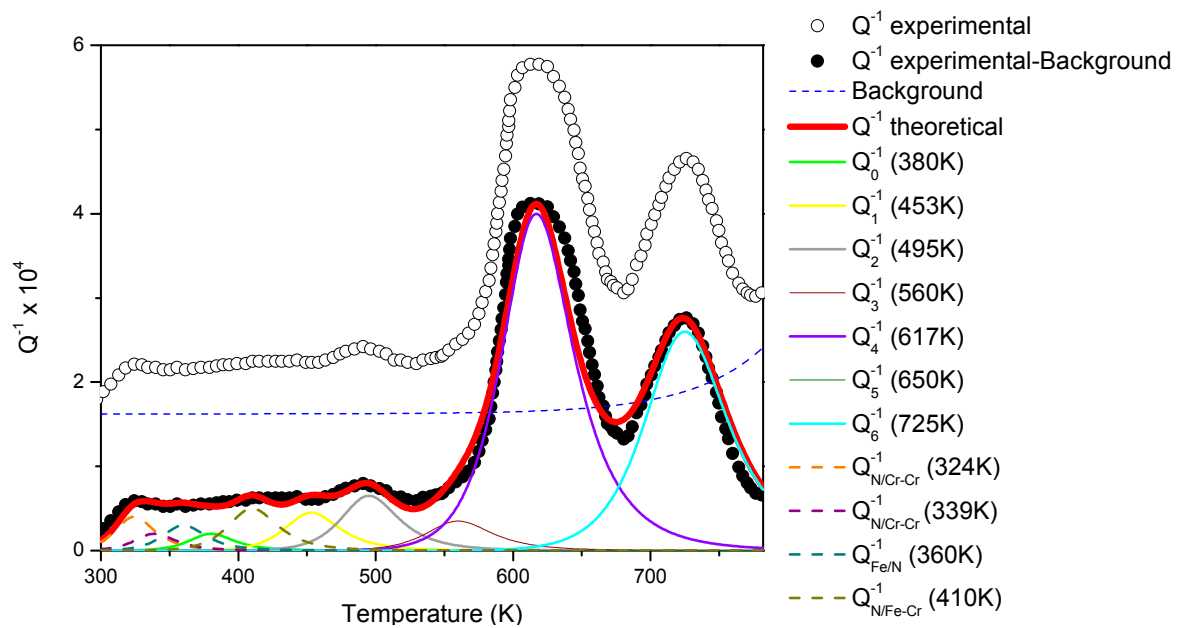
Table 3. Peak positions (T) and relaxation strengths (Δ) used to fit experimental data in Figure 4.

| T, Δ	C Peaks							N Peaks			
	C–Cr$_0$	C–Cr$_1$	C–Cr$_2$	C–Cr$_3$	C–Cr$_4$	C–Cr$_5$	C–Cr$_6$	N/Cr–Cr	N/Cr–Cr	Fe/N	N/Fe–Cr
Figure 4a											
T (K)	380	453	500	560	617	650	714	324	339	360	410
$\Delta \times 10^4$	0.65	0.4	1.3	0	4.9	0	1.25	0.7	0.85	0.45	0.55
Figure 4b											
T (K)	380	453	495	560	617	650	725	324	339	360	410
$\Delta \times 10^4$	0.2	0.45	0.65	0.35	4	0	2.6	0.4	0.2	0.3	0.5
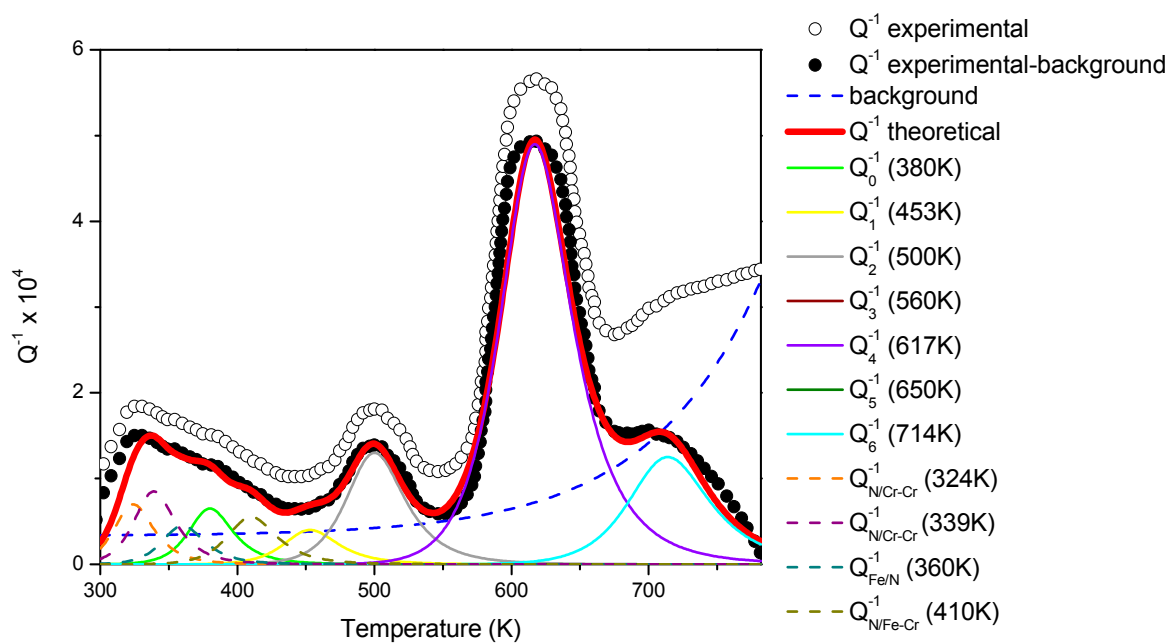
(**a**)

Figure 4. *Cont.*

(**b**)

Figure 4. Fitting of the Q^{-1} curves of the steel quenched from 1348 K with cooling rates of 3600 K/min (**a**) and 150 K/min (**b**). The best fit curve is the sum of the background curve, seven peaks corresponding to C–Cr associates with *i* values from 0 to 6, and four peaks due to N.

3.2. Cr Segregation Phenomena

Different cooling rates from the austenitic field (1348 K) do not seem to have effects on the microstructure and mechanical properties of the steel, however, successive steps of tempering treatment determine a quite different behaviour, in particular, of the fracture mode. Figure 5, re-drawn from ref. [22], compares the ductile to brittle transition temperature (DBTT) of samples quenched from 1348 K with cooling rates of 150 and 3600 K/min and, then, submitted to heat treatments at 973 K for increasing time. DBTT was determined from Charpy tests performed on standard V-notched probes in the temperature range from 173 K (−100 °C) to + 423 K (+150 °C).

After quenching, DBTT is 285 K (+12 °C) for both materials, however, the curves exhibit a different trend as the time of tempering treatment at 973 K increases. In the case of the samples quenched at 150 K/min, a minimum is observed after 2 hours, followed by a maximum at 6 hours, and by a progressive decrease for longer tempering time. On the contrary, DBTT of the samples quenched at 3600 K/min shows an initial decrease (up to 4 h), then it remains substantially stable.
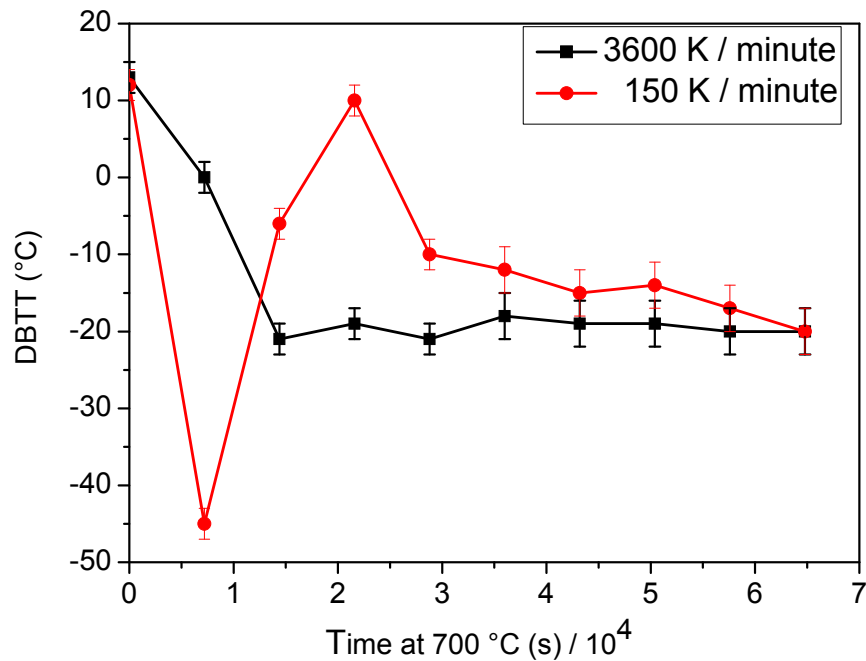
Figure 5. DBTT of the Cr martensitic steel vs. time of heat treatment at 973 K: Comparison of samples quenched from 1348 K with two cooling rates (150 and 3600 K/min).

SEM observations on fracture surfaces of probes broken in ductile field showed no significant differences in samples cooled with different rates. In brittle field, the morphological features for both the materials in as-quenched condition are the same, namely, those typical of a quasi-cleavage fracture, but differences arise and become gradually more pronounced at increasing time of tempering. After 7.2×10^4 s (20 h) at 973 K, the fracture surfaces of samples cooled at 3600 and 150 K/min show different morphologies (Figure 6): the fracture mode is always of quasi-cleavage in (Figure 6a), whereas is mixed (quasi-cleavage plus intercrystalline) in (Figure 6b).
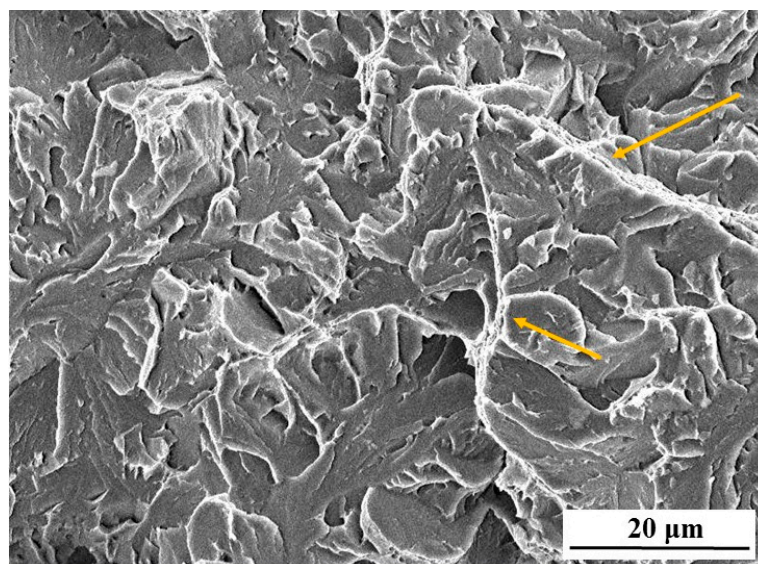
(**a**)

Figure 6. *Cont.*
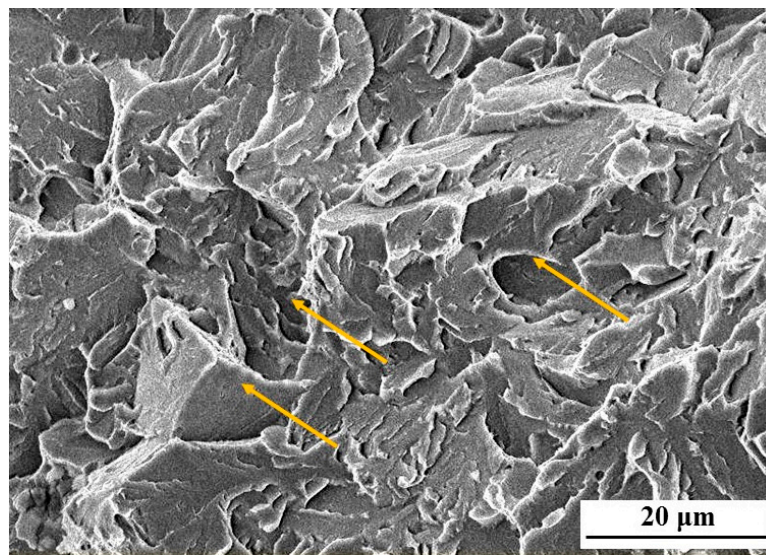
(**b**)

Figure 6. Fracture surfaces of samples treated 20 h at 973 K, and broken in Charpy tests at 233 K (−40 °C), namely, in the brittle field: quenching rate from austenitic field of 3600 K/min (**a**) and 150 K/min (**b**). Arrows indicate tear ridges in (**a**), and the zones with intercrystalline fracture morphology in (**b**).

The image of Figure 6a shows the typical quasi-cleavage fracture surface: the cracks are multiple and transgranular, with tear ridges in the zones where moving cracks join together. A similar morphology is observed in Figure 6b, however, in this case, zones are also present where the fracture front travelled along the boundaries of primary austenitic grains (typical features of intercrystalline fracture). In fact, the fracture is mixed, occurring in both quasi-cleavage and intercrystalline modes.

The different evolution of the two materials, whose microstructure and mechanical properties after quenching are apparently similar, has been related to the different C–Cr associates distribution shown in Figure 1, namely, large numbers of C–Cr associate with $i = 4$ and 2 after faster cooling, $i = 4$ and 6 after slower cooling. Both cases are consistent with an original Cr clustering in austenitic field (before cooling), which exhibits a specific evolution depending on cooling rate. Cr clustering in austenite was examined in detail in a previous work [15]. Monte Carlo simulations demonstrated that Cr clustering occurs through a two-step process owing to the different diffusivities of C and Cr: 1st step—rapid diffusion of C atoms to form C–Cr associates, 2nd step—slower diffusion of Cr leading to the C–Cr associates coalescing, giving rise to Cr-rich clusters.

Figure 7 shows the Q^{-1} curves of samples quenched at 3600 and 150 K/min, and treated at 973 K for 3.6×10^4 s (10 h) and 7.2×10^4 s (20 h). The curves of the steel quenched with the faster cooling rate (Figure 7a,b) do not show relevant variations after the heat treatments, and maintain prevalent peaks referable to C–Cr associates with $i = 2$ and $i = 4$, like that of as-quenched steel (see Figure 4a and Table 3).

On the contrary, those of the steel cooled at a rate of 150 K/min (Figure 7c,d) significantly change in two particular branches, at lower and higher temperature (substantially below or above 500 K), and can be distinguished referable to the occurrence of Cr-depleted and Cr-enriched zones, respectively (see Table 4).

From the results, it is clear that the C–Cr associates distribution depends on the cooling rate from austenitic field; the distribution obtained with the lower cooling rate is not stable, and evolves when the material is heat treated at 973 K, giving rise to zones with different Cr content, i.e., Cr segregation. In particular, Cr segregation at grain boundaries is connected to phenomena of embrittlement and DBTT variations (see Figure 5). The distribution of C–Cr associates in the steel, submitted to the

higher cooling rate, is substantially stable, thus, segregation does not take place and, consequently, the mechanical behaviour is not affected by intercrystalline ruptures.
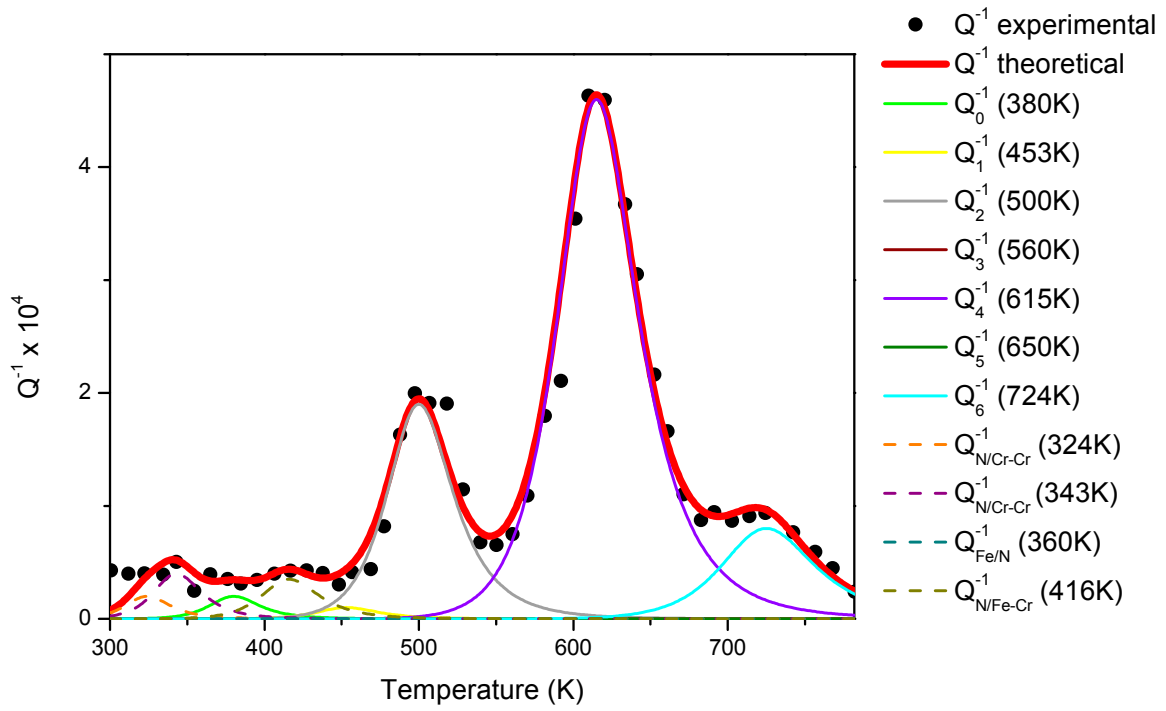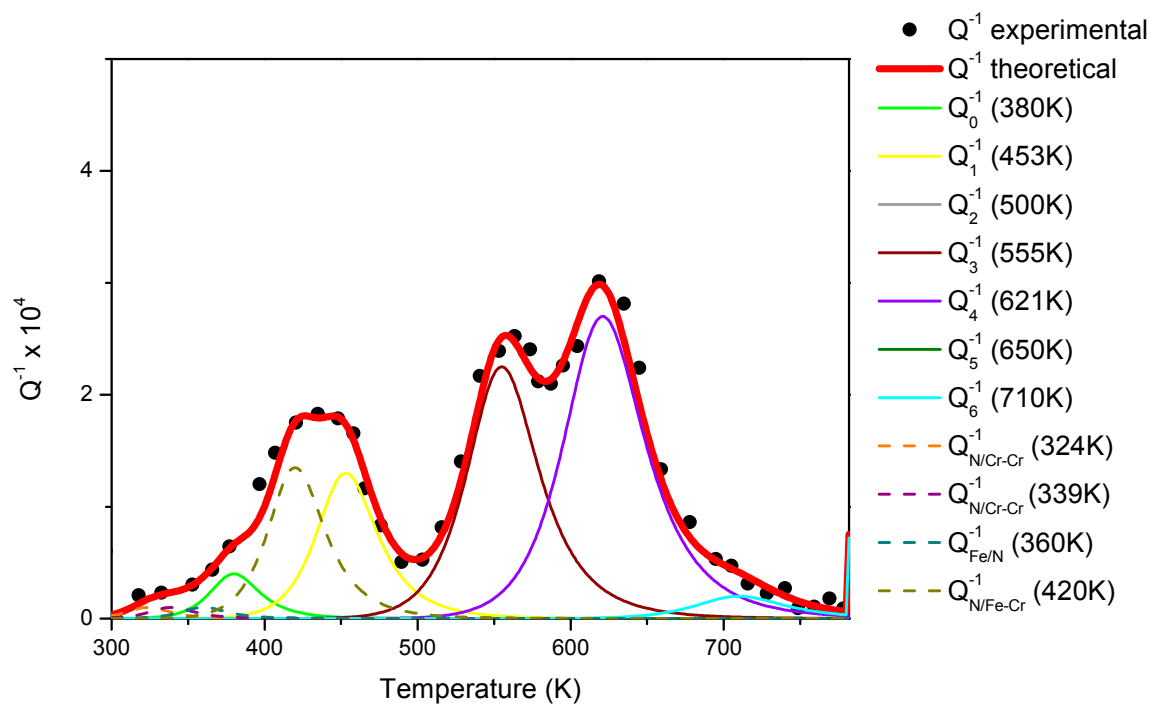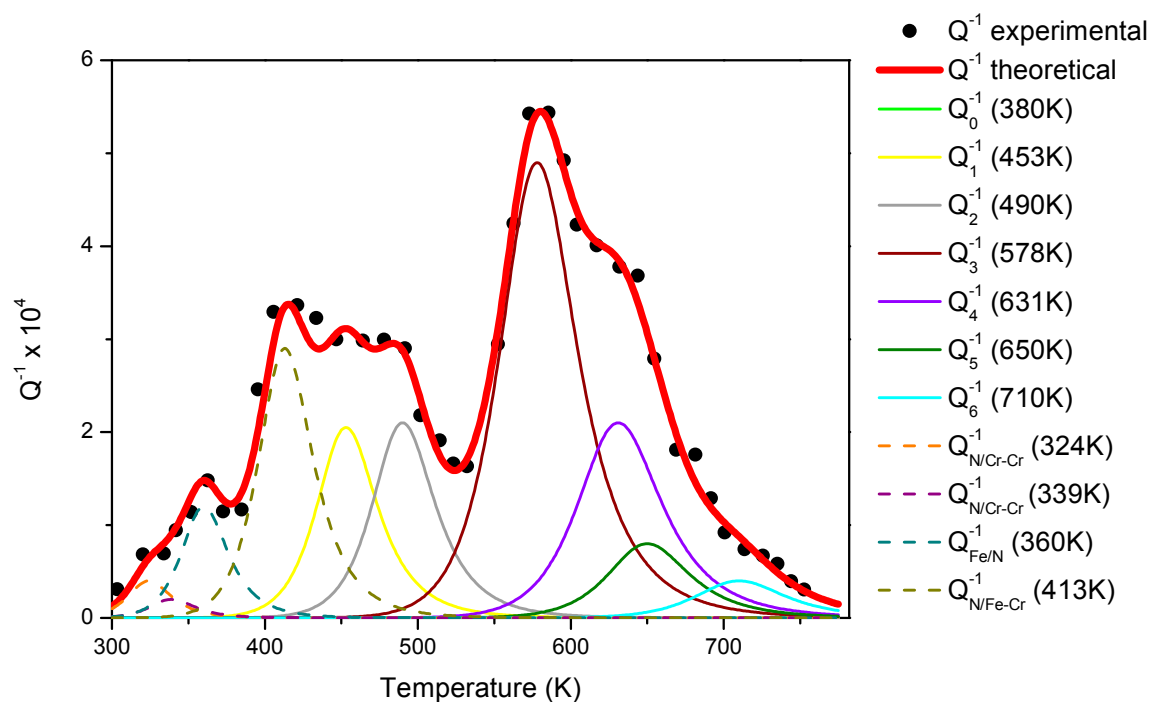

(**a**)
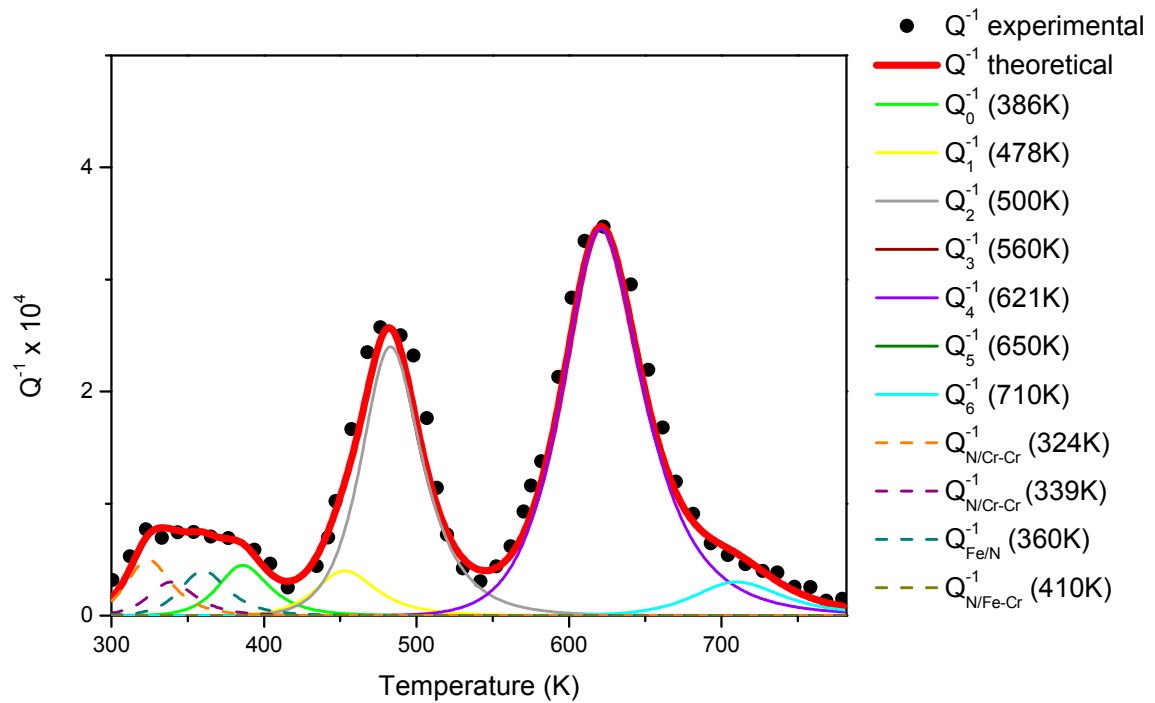
(**b**)

Figure 7. *Cont.*

(**c**)

(**d**)

Figure 7. Q^{-1} curves of samples quenched at 3600 (**a**,**b**) and 150 K/min (**c**,**d**), and treated at 973 K for 3.6×10^4 s (**a**,**c**) and 7.2×10^4 s (**b**,**d**). Experimental data are reported after background subtraction.

Table 4. Temperatures T and relaxation strengths Δ of the Q^{-1} peaks used to fit MS experimental data displayed in Figure 7, quenched at 3600 (Figure 7a,b) and 150 K/min (Figure 7c,d), and treated at 973 K for 3.6×10^4 s (Figure 7a,c) and 7.2×10^4 s (Figure 7b,d).

T, Δ	C Peaks							N Peaks			
	C–Cr$_0$	C–Cr$_1$	C–Cr$_2$	C–Cr$_3$	C–Cr$_4$	C–Cr$_5$	C–Cr$_6$	N/Cr–Cr	N/Cr–Cr	Fe/N	N/Fe–Cr
Figure 7a											
T (K)	380	453	500	560	615	650	724	324	343	360	416
$\Delta \times 10^4$	0.2	0.1	1.9	0	4.6	0	0.8	0.2	0.4	0	0.35
Figure 7b											
T (K)	386	453	483	560	621	650	710	324	339	360	410
$\Delta \times 10^4$	0.45	0.4	2.4	0	3.45	0	0.3	0.5	0.3	0.4	0
Figure 7c											
T (K)	380	453	500	555	621	650	710	324	339	360	420
$\Delta \times 10^4$	0.4	1.3	0	2.25	2.7	0	0.2	0.1	0.1	0.1	1.35
Figure 7d											
T (K)	380	453	490	578	631	650	710	324	339	360	413
$\Delta \times 10^4$	0	2.05	2.1	4.9	2.1	0.8	0.4	0.4	0.2	1.2	2.9

3.3. Interaction of Hydrogen with C–Cr Associates

Hydrogen in steels represents the cause of severe failures in mechanical components. Hydrogen embrittlement (HE) and hydrogen attack (HA) are different phenomena related to the presence of hydrogen in steels, and both of them have detrimental effects.

HE decreases the ductility, toughness, true stress at fracture, and accelerates crack growth [31–34], leading to catastrophic failure or delayed rupture of structural materials. Hydrogen can be pre-existing in the matrix, or picked up from the environment; in any case, HE effects depend on the concentration, temperature, composition, and microstructure of the material. Turnbull et al. [35] analysed the combined effects of reversible and irreversible trap sites on hydrogen transport in Cr martensitic steels. Typical HE mechanisms are bubble formation, reduction in lattice cohesive forces, reduction in surface energy, and hydride formation.

HA is an irreversible process, occurring only above 473 K, and consists in the reaction of H with C to form methane (CH_4). The phenomenon, described and discussed in a classical paper by Shewmon [36], causes swelling and brittle behaviour in plain carbon steels, whereas it does not occur in Cr steels if the Cr content is higher than 7%. Lacombe et al. [37] demonstrated by means of autoradiographic technique that HE is suppressed because H concentrates around Cr-enriched grain boundaries and Cr carbides. The problem investigated here regards HA: how do C–Cr associates interact with H introduced into the steel at high temperature?

The steel has been submitted to an austenitisation treatment at 1348 K for 7.2×10^3 s (2 h), and cooled to room temperature with a rate of 150 K/min. To examine the effect of H permeation on the material in different conditions, two sets of samples have been examined by MS measurements: as-quenched and annealed for 7.2×10^4 s (20 h) at 973 K. Both sets have been H-permeated by a three-step treatment consisting of (i) heating up to 873 K at a rate of 6.7×10^{-3} K/s, (ii) permeation at 873 K for 8.6×10^5 s in flowing gas with a pressure of 10^5 Pa, (iii) cooling down to room temperature at the same rate used for heating. MS measurements were carried out on both sets of samples before and after H permeation.

Q^{-1} curves of the steel, quenched and H-permeated (QH), quenched and annealed (QA), quenched, and annealed and H-permeated (QAH), are reported in Figure 8. Experimental data are reported after background subtraction.
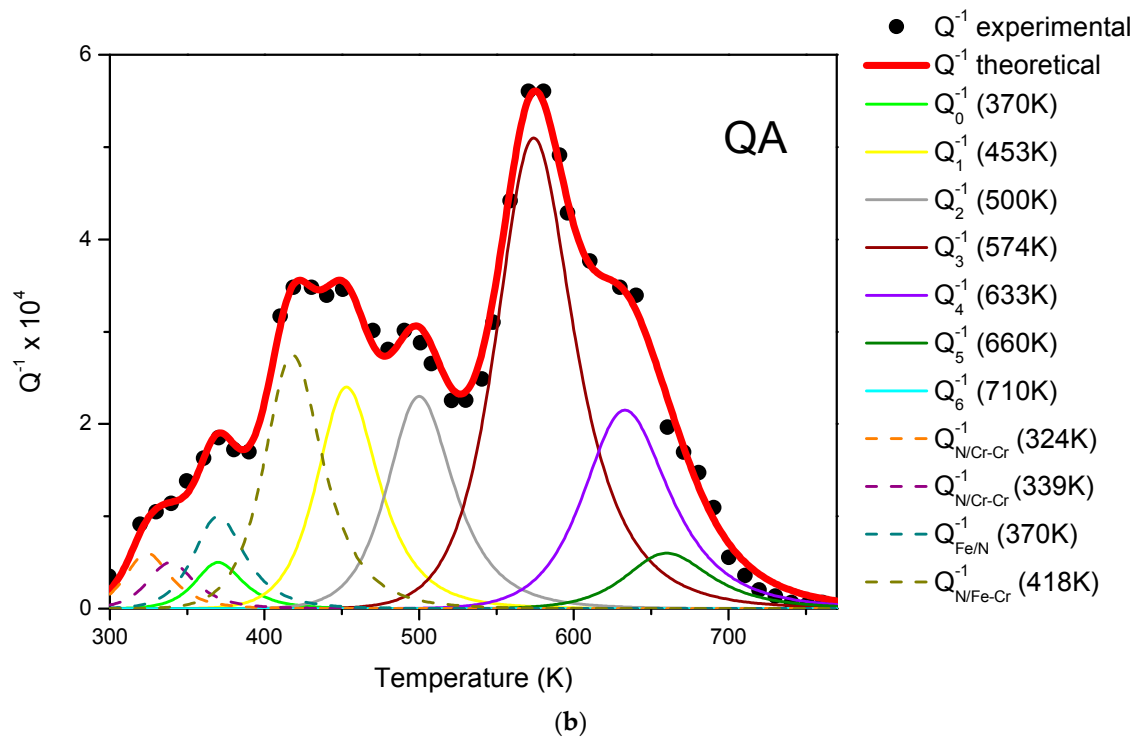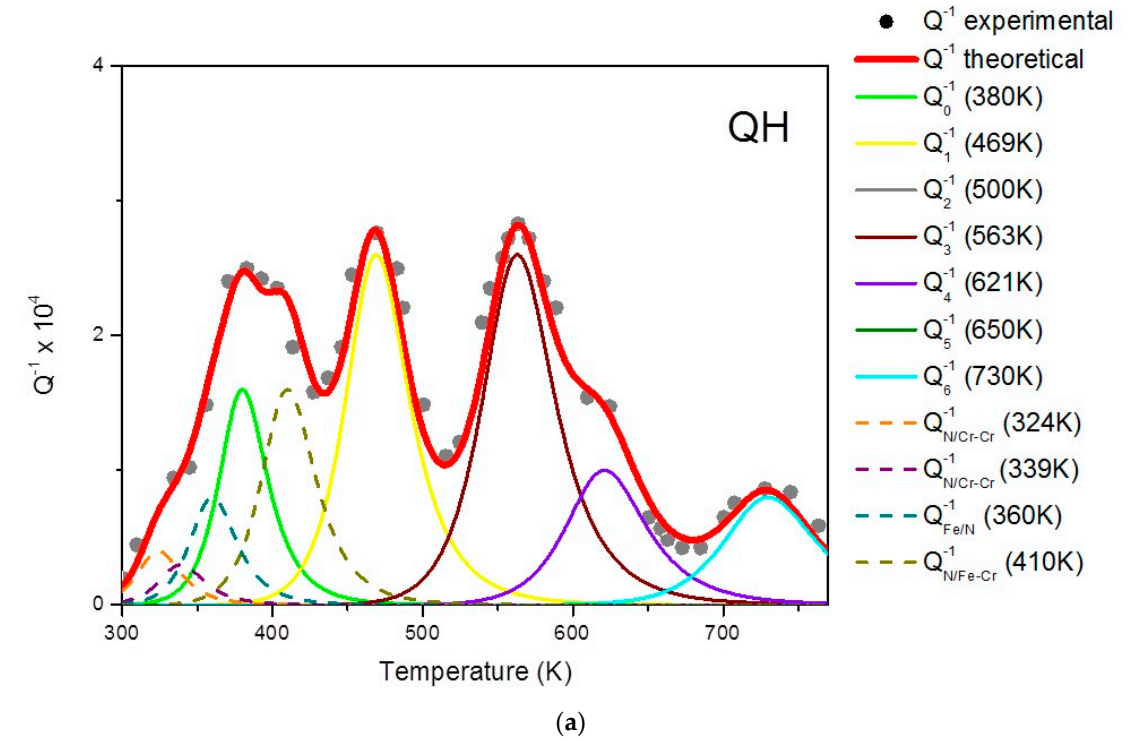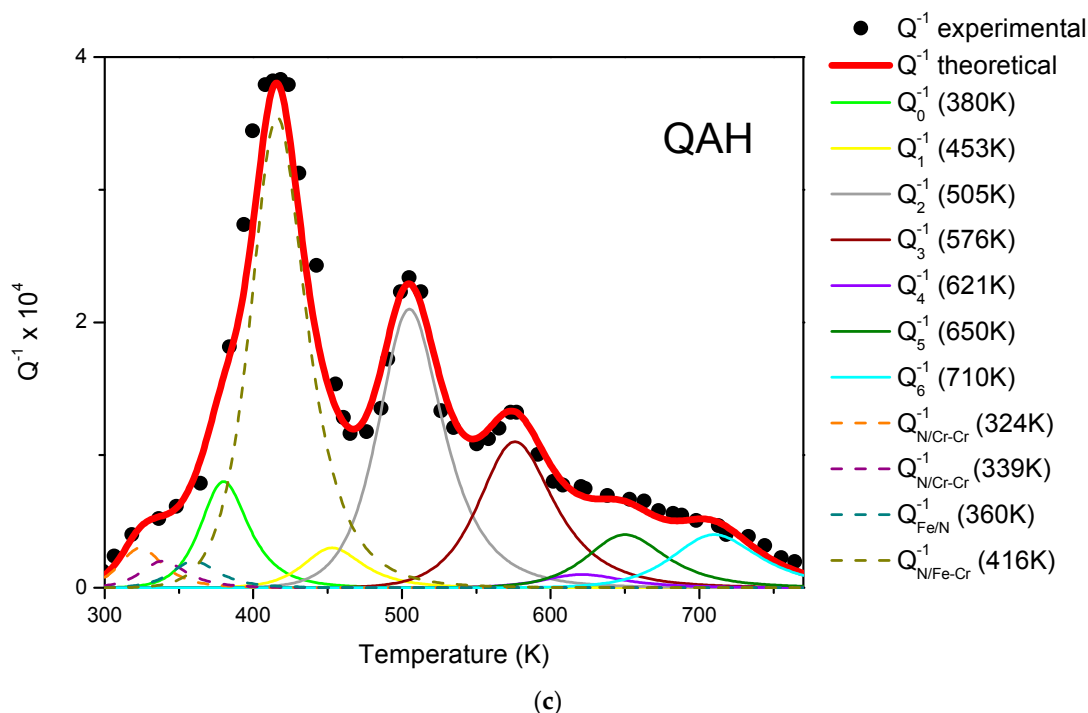
(**a**)

(**b**)

Figure 8. *Cont.*

(**c**)

Figure 8. Q^{-1} spectra of the steel, quenched and H-permeated (**QH**), quenched and annealed (**QA**), quenched, and annealed and H-permeated (**QAH**). Experimental data are reported after background subtraction.

The relaxation strengths of the peaks used to fit the curves in Figure 8 are reported in Table 5. The Q^{-1} curve of the quenched (Q) steel is displayed in Figure 4b, and the corresponding data are reported in Table 3 and, also, in Table 5, to make the comparison easier.

Table 5. Temperatures T and relaxation strengths Δ of the Q^{-1} peaks used to fit MS experimental data displayed in Figure 8, for the samples quenched (Q), quenched and H-permeated (QH), quenched and annealed (QA), and quenched, annealed, and H-permeated (QAH). Data of the quenched (Q) steel (Table 3) are also reported for comparison.

T, Δ	C Peaks							N Peaks			
	C–Cr$_0$	C–Cr$_1$	C–Cr$_2$	C–Cr$_3$	C–Cr$_4$	C–Cr$_5$	C–Cr$_6$	N/Cr–Cr	N/Cr–Cr	Fe/N	N/Fe–Cr
Figure Q											
T (K)	380	453	495	560	617	650	725	324	339	360	410
$\Delta \times 10^4$	0.2	0.45	0.65	0.35	4	0	2.6	0.4	0.2	0.3	0.5
Figure QA											
T (K)	370	453	500	574	633	660	710	324	339	370	418
$\Delta \times 10^4$	0.5	2.4	2.3	5.1	2.15	0.6	0	0.6	0.5	1	2.75
Figure QH											
T (K)	380	469	500	563	621	650	730	324	339	360	410
$\Delta \times 10^4$	1.6	2.6	0	2.6	1	0	0.8	0.4	0.3	0.8	1.6
Figure QAH											
T (K)	380	453	505	576	621	650	710	324	339	360	416
$\Delta \times 10^4$	0.8	0.3	2.1	1.1	0.1	0.4	0.4	0.3	0.2	0.2	3.55

As shown in Figure 8 and Table 5, H permeation changes the relaxation strengths Δ of Q^{-1} peaks, and the total amount of C and N atoms giving rise to relaxation processes.

From the comparison of the relaxation strengths of the as-quenched steel before and after H permeation, it is evident that the amount of interstitials (C and N) involved in relaxation processes is higher in H-charged samples. The total amount of interstitials contributing to relaxation processes is proportional to the area under the Q^{-1} curve, and the ratio between the areas of Q and QH samples is 0.97. The increasing amount of C and N atoms contributing to relaxation processes depends on

the martensitic structure evolution. As-quenched martensite consists of laths with a high density of dislocations (~10^{11} cm^{-2}); such microstructure changes if the material is treated at the temperature of 873 K involved in H permeation, in particular, laths disappear, and dislocation density strongly decreases [38]. Since laths and dislocations are sinks for interstitials, a large number of C and N atoms become free and, consequently, even if a part of them forms carbides and nitrides, and another part is bound by H atoms, the overall effect of H permeation treatment is to increase the amount of interstitial atoms participating in anelastic processes.

A different behaviour is exhibited by the samples annealed for 7.2×10^4 s at 973 K: the ratio between the areas under the Q^{-1} curves of QA and QAH samples is 2.03. In this case, the material has, in origin, a fully recovered structure, and the precipitation of carbides and nitrides has been substantially completed [38], therefore, C and N atoms contributing to relaxation peaks decrease, due to the H blocking effect.

It is noteworthy that the relative intensities of Q^{-1} peaks, due to C–Cr clusters with a higher number of Cr atoms, are strongly reduced after H permeation in both as-quenched (Q) and quenched and annealed steels (QA). In as-quenched steel, the intensities of the Q^{-1}_6 and Q^{-1}_4 peaks decrease from 2.6×10^{-4} and 4.0×10^{-4} (Q) to 0.8×10^{-4} and 1.0×10^{-4} (QH), respectively, while in quenched and annealed samples, the relaxation strengths of Q^{-1}_4 and Q^{-1}_3 peaks pass from 2.15×10^{-4} and 5.1×10^{-4} (QA) to 0.1×10^{-4} and 1.1×10^{-4} (QAH).

Each relaxation process consists of the alternative jumping of a single interstitial atom from an octahedral position to another one. If an atom of C is bound to an atom of H, it is no more able to jump because the process would not involve the single C atom, but the C–H pair with a tremendous lattice distortion. Since C atoms strongly bound by H atoms are hindered to participate in relaxation processes, the intensities of the corresponding Q^{-1}_6 peaks are expected to decrease. Therefore, MS results indicate that a preferred interaction between H atoms and C–Cr associates with a high number of Cr atoms does exist. These associates play a significant role in HA mechanism because, if H atoms are attracted and bound by C–Cr associates, they are not able to diffuse towards grain boundaries, sub-boundaries, and dislocation tangles where CH$_4$ bubbles could nucleate (first stage of HA), grow, merge and, finally, form fissures and cracks (final stage of HA).

In conclusion, the present experiments demonstrate how C–Cr associates with a high number of Cr atoms contribute, together with Cr carbides and Cr-enriched boundaries, to block H atoms and suppress HA. The result is in agreement with the existence of a critical limit, around 7%, below which the Cr amount is not sufficient to avoid H attack. As a matter of fact, the Q^{-1} peaks corresponding to C–Cr associates with a high number of Cr atoms are absent in the curves of low Cr steels (see ref. [30]).

3.4. Nucleation of Cr Carbides

The aim of the present work is to determine whether the C–Cr associates affect the precipitation of Cr carbides and, in this case, to assess their specific role in the process.

The samples underwent austenitisation treatment (1.8×10^3 s at 1348 K), then, were cooled to room temperature at a rate of 150 K/min, and subjected to a multi-step heat treatment consisting of successive steps of 3.6×10^3 s at 673, 773, and 873 K. MS measurements have been carried out on the same samples after each heating step, while a set of different samples were used for destructive tests (carbide extraction). The examined temperature range is that of M$_7$C$_3$ and M$_{23}$C$_6$ carbides (M = metal, C = carbon) precipitation.

Carbides were extracted from the metallic matrix through an electrochemical method. For example, Figure 9 shows the carbides extracted after the heating step at 873 K. The SEM image displays some squared particles (side ~7–8 μm), and a lot of small round particles (~0.1 μm); EDS microanalysis showed that the larger particles are rich in Cr, while those of smaller size are rich in Nb.
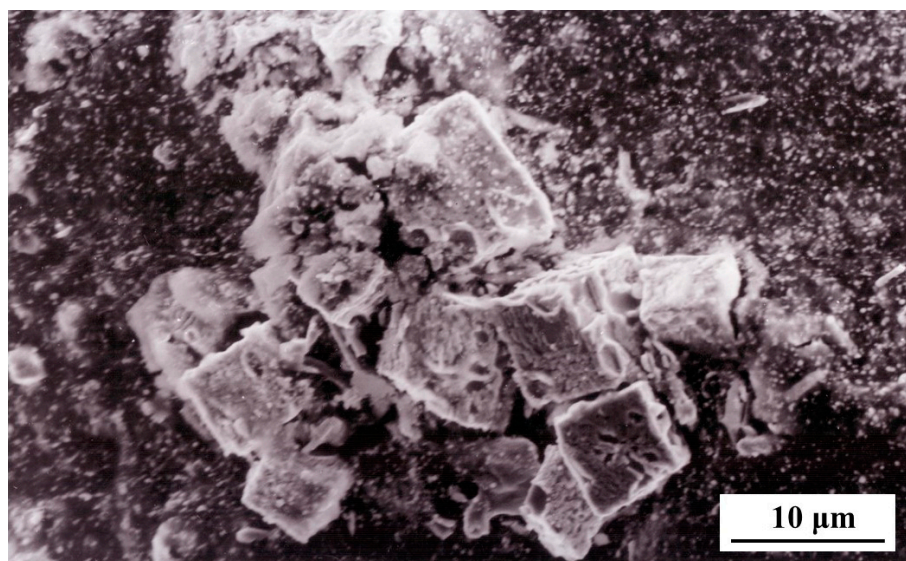
Figure 9. SEM image of the carbides extracted after the heating step at 873 K.

From XRD spectra, the carbides have been identified using the JCPDS-ICDD database [39]:

i.   NbC, cubic ($a = 0.44698$ nm), JCPDS-ICDD file 38–1364,
ii. Nb_2C, orthorhombic ($a = 1.0920$ nm, $b = 0.4974$ nm, $c = 0.3000$ nm), JCPDS-ICDD file 19–858,
iii. Cr_7C_3, hexagonal ($a = 1.398$ nm, $c = 0.452$ nm), JCPDS-ICDD file 11–550,
iv. $Cr_{23}C_6$, cubic ($a = 1.066$ nm), JCPDS-ICDD file 35–783.

In fact, the XRD peaks exhibit small shifts with respect to the angular positions reported by the database, because it refers to monometallic carbides whereas, in the present case (see Table 6), carbides contain also other elements in addition to the main ones (Nb and Cr). Therefore, the crystal structure is the same, but lattice plane distances are a little changed.

**Table 6.** EDS measurements: Average atomic fractions of metals present in the extracted carbides.

Carbides Type	Cr (atom %)	Fe (atom %)	Nb (atom %)	Mo (atom %)
NbC	3	8	79	10
Nb_2C	1	1	91	7
Cr_7C_3	50	45	3	2
$Cr_{23}C_6$	63	28	4	5

Table 7 summarises the XRD results and reports the most intense reflections of the carbides extracted after each heating step and their relative intensities. Only the XRD reflections of Nb-rich carbides (NbC and Nb_2C) are present after the 673 K heating step. These carbides, already present in austenitic field, are retained after quenching, and are substantially unaffected by the treatments in the examined temperature range. After the step at 773 K, M_7C_3 Cr-rich carbides form, whereas $M_{23}C_6$ carbides appear after the 873 K step. The change in relative intensities of XRD reflections indicate that the precipitation of $M_{23}C_6$ takes place at the expense of M_7C_3 carbides.

Table 7. Angular positions Θ and relative intensities I/I_0 of the XRD reflections of carbides extracted from samples heat treated up to 673, 773, and 873 K.

Treatment Temperature	673 K		773 K		873 K	
Θ (deg)	Carbide type	I/I_0	Carbide type	I/I_0	Carbide type	I/I_0
7.620	M_2C (400)	35	M_2C (400)	28	M_2C (400)	58
7.900	MC (111)	100	MC (111)	100	MC (111)	100
8.610	M_2C (211)	33	M_2C (211)	27	M_2C (211)	60
8.995	M_7C_3 (411)	-	M_7C_3 (411)	20	M_7C_3 (411)	-
9.130	MC (200)	74	MC (200)	77	MC (200)	70
9.380	$M_{23}C_6$ (422)	-	$M_{23}C_6$ (422)	-	$M_{23}C_6$ (422)	32
9.950	$M_{23}C_6$ (511)	-	$M_{23}C_6$ (511)	-	$M_{23}C_6$ (511)	42
12.635	$M_{23}C_6$ (511)	-	$M_{23}C_6$ (511)	-	$M_{23}C_6$ (511)	28
12.650	M_7C_3 (332)	-	M_7C_3 (332)	17	M_7C_3 (332)	-
12.970	MC (220)	40	MC (220)	44	MC (220)	42
14.550	M_2C (231)	28	M_2C (231)	11	M_2C (231)	19
15.460	M_7C_3 (641)	-	M_7C_3 (641)	17	M_7C_3 (641)	5
16.045	M_7C_3 (423)	-	M_7C_3 (423)	13	M_7C_3 (423)	4

Figure 10a–c compares the Q^{-1} spectra after successive heating steps; each spectrum has been fitted according to the aforesaid analysis procedure, and the different relaxation strengths are displayed. Also, in this case, experimental data are reported after background subtraction. In general, it can be observed that the spectra undergo relevant changes depending on the heat treatment temperature with variations of the peak relaxation strengths (see Table 8).
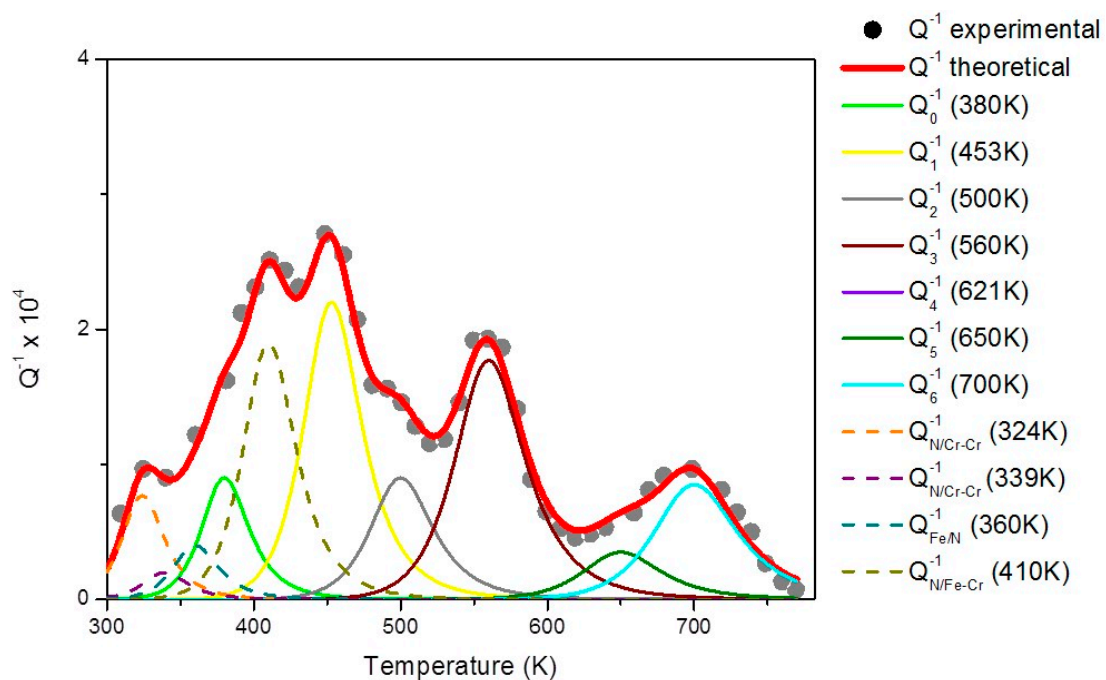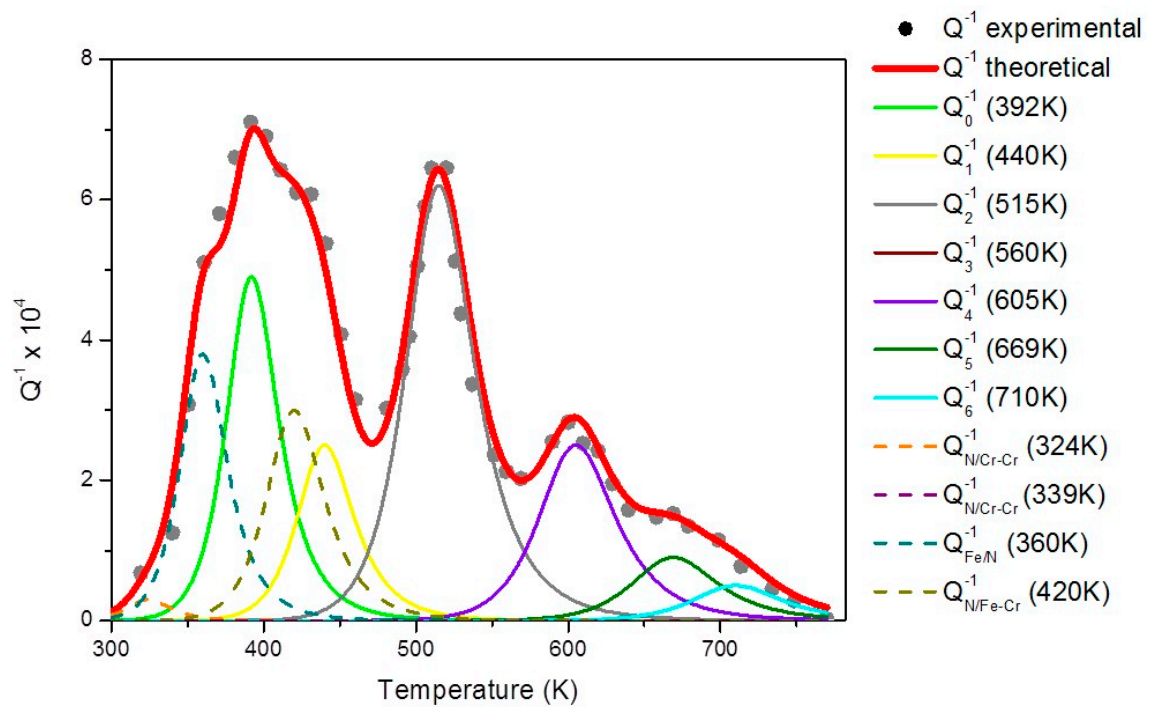

(a)

Figure 10. *Cont.*
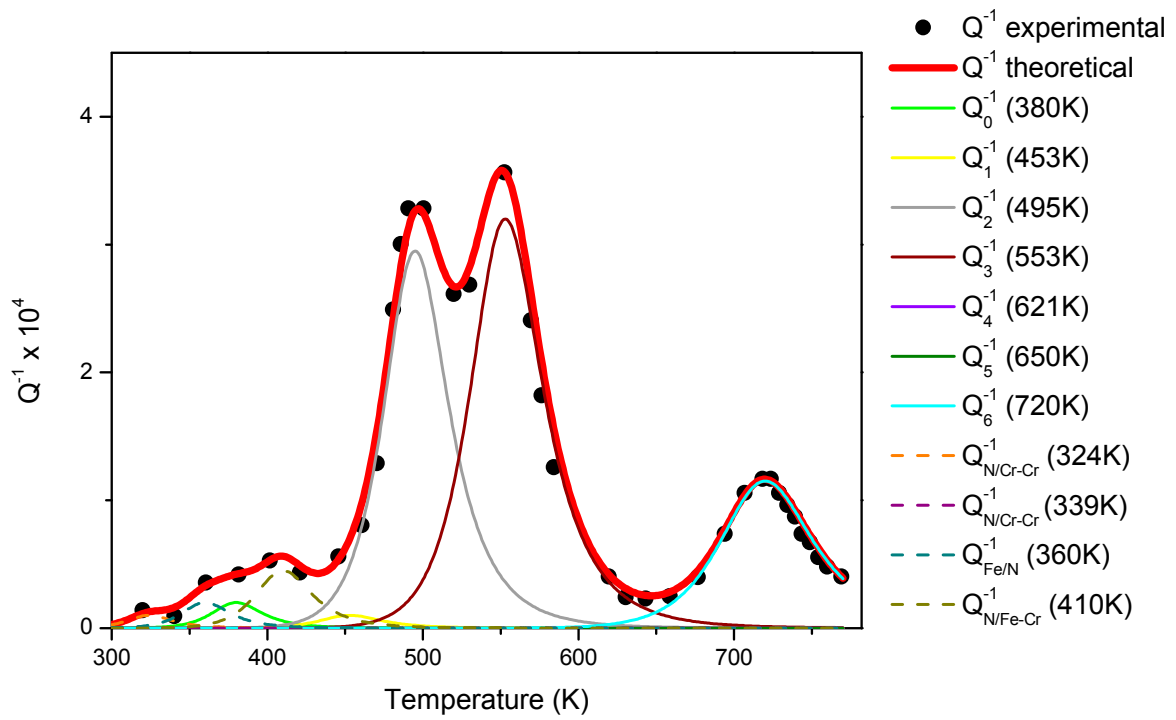
(**b**)

(**c**)

Figure 10. Q^{-1} curves after successive heating steps at 673 K (**a**), 773 K (**b**), and 873 K (**c**). Experimental data are reported after background subtraction.

Table 8. Temperatures T and relaxation strengths Δ of the Q^{-1} peaks used to fit MS experimental data displayed in Figure 10 for the samples heat treated up to 673, 773, and 873 K.

T, Δ	C Peaks							N Peaks			
	C–Cr$_0$	C–Cr$_1$	C–Cr$_2$	C–Cr$_3$	C–Cr$_4$	C–Cr$_5$	C–Cr$_6$	N/Cr–Cr	N/Cr–Cr	Fe/N	N/Fe–Cr
Figure 10a											
T (K)	380	453	500	560	621	650	700	324	339	360	410
Δ × 10^4	0.9	2.2	0.9	1.77	0	0.35	0.85	0.77	0.2	0.4	1.9
Figure 10b											
T (K)	380	453	495	553	621	650	720	324	339	360	410
Δ × 10^4	0.2	0.1	2.95	3.2	0	0	1.15	0.1	0	0.2	0.45
Figure 10c											
T (K)	392	440	515	560	605	669	710	324	339	360	420
Δ × 10^4	4.9	2.5	6.2	0	2.5	0.9	0.5	0.3	0	3.8	3

The results indicate that the distribution of C–Cr associates is altered by treatments at increasing temperature. It is noteworthy that the most intense Q^{-1} peak after the 673 K treatment, namely, that connected with associates with 1 Cr atom, completely disappears after the successive step at 773 K, and reappears after the 873 K one. Such behaviour is clearly related to the precipitation of Cr-rich carbides in this range of temperatures.

EDS results in Table 6 show that the composition of Cr_7C_3 carbides consist of 50% Cr atoms, thus, the ratio between C and Cr atoms is about 1:1. In concomitance with Cr_7C_3 carbides precipitation at 773 K, the Q^{-1} peak due to relaxation of C–Cr associates with 1 Cr atom, which is the most intense after treatment at 673 K, becomes very low, indicating that these associates do not contribution more to relaxation. Therefore, Cr_7C_3 formation seems to occur through a process involving these types of associates. On these grounds, it is supposed that C–Cr$_1$ associates may directly aggregate to form Cr_7C_3 carbides.

The hypothesis of carbide formation through C–Cr$_1$ aggregation is consistent with the Cr_7C_3 structure described by Dyson and Andrews [40]. The positions occupied by metal and C atoms in the Cr_7C_3 carbide cell are displayed in Figure 11: different atomic layers are indicated by specific symbols, and the complex structure consists of distorted octahedra having a C atom at the centre (one of them is indicated).
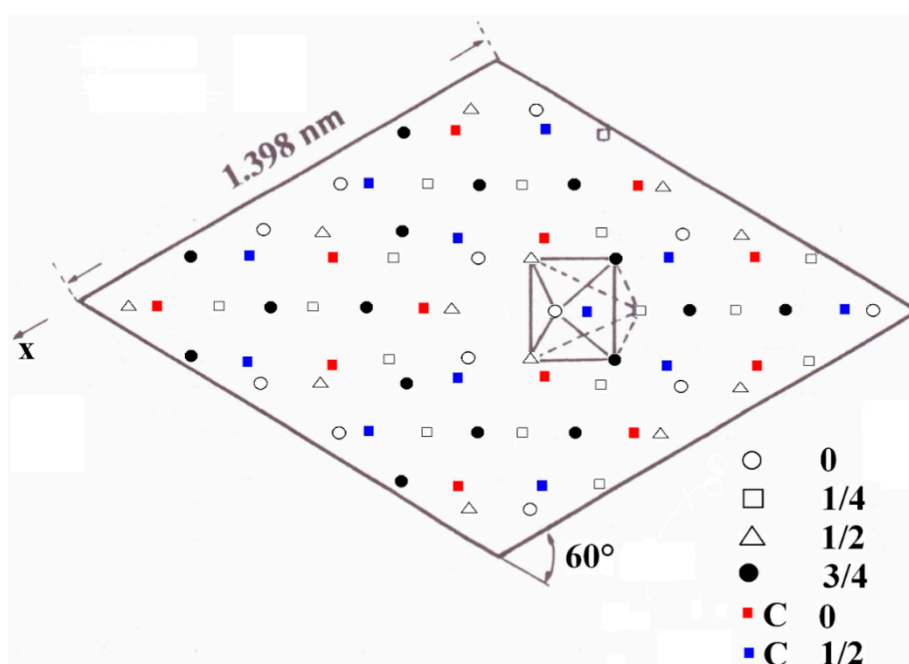
Figure 11. Cr_7C_3 carbide cell according to Dyson and Andrews [40].

Following the 873 K heat step, $Cr_{23}C_6$ carbides form at expenses of Cr_7C_3 carbides, but nucleate on different sites [41]. When Cr_7C_3 carbides solve, C–Cr_1 associates are released in the matrix, can thus participate again to relaxation processes, and the corresponding Q^{-1} peak is observed in the spectrum (Figure 10c).

4. Conclusions

This work presents the results of MS experiments carried out on a Cr martensitic steel. The Q^{-1} vs. temperature curves have been analysed by considering all the relaxation processes involving C and N interstitial atoms. The point defects exhibit different configurations with Cr atoms, which strongly affect the microstructure evolution and mechanical behaviour. The role played by point defects is relevant, and can be summarised as follows:

(i) Cr segregation depends on C–Cr associates distribution in as-quenched material: slow cooling rate from austenitic field involves an unstable distribution which evolves after tempering at 973 K, leading to Cr concentration fluctuations. The phenomenon, which affects the brittle mode of fracture, does not occur if the material is quenched at a higher cooling rate.

(ii) Hydrogen interacts with C–Cr associates, in particular, those which have a high number of Cr atoms. The phenomenon plays a significant role in HA mechanism because H atoms bound by C–Cr associates are not able to diffuse towards lattice defects (grain boundaries, sub-boundaries, and dislocation tangles) where CH_4 bubbles nucleate and successively grow and merge, to form the HA typical cracks.

(iii) C–Cr associates take part in the nucleation mechanism of Cr_7C_3 carbides, and specifically these carbides form by the aggregation of C–Cr associates with 1 Cr atom.

Author Contributions: R.M. planned the experiments; A.V. prepared the samples; R.M. and A.V. performed MS tests; A.F. made the analysis of Q^{-1} spectra; all the authors contributed to analysing the results and writing the manuscript.

References

1. Schultz, H. Point defects in body-centred cubic transition metals. *Mater. Sci. Eng.* **1968**, *3*, 189–219. [CrossRef]
2. Townsend, J.R.; Di Carlo, J.A.; Nielsen, R.L.; Stabell, D. The elastic bulk effect of point defects in metals. *Acta Metall.* **1969**, *17*, 425–435. [CrossRef]
3. Lutsko, J.F.; Wolf, D.; Phillpot, S.R.; Yip, S. Molecular-dynamics study of lattice-defect-nucleated melting in metals using an embedded-atom-method potential. *Phys. Rev. B* **1989**, *40*, 2841–2855. [CrossRef]
4. Granato, A.V. Interstitialcy model for condensed matter states of face-centered-cubic metals. *Phys. Rev. Lett.* **1992**, *68*, 974–977. [CrossRef] [PubMed]
5. Gordon, C.A.; Granato, A.V. Equilibrium concentration of interstitials in aluminum just below the melting temperature. *Mat. Sci. Eng. A* **2004**, *370*, 83–87. [CrossRef]
6. Montanari, R. Real-time XRD investigations on metallic melts. *Int. J. Mater. Prod. Tech.* **2004**, *20*, 452–463. [CrossRef]
7. Montanari, R.; Varone, A. Synergic role of self-interstitials and vacancies in Indium melting. *Metals* **2015**, *5*, 1061–1072. [CrossRef]
8. Goncharova, E.V.; Makarov, A.S.; Konchakov, R.A.; Kobelev, N.P.; Khonik, V.A. Premelting generation of interstitial defects in polycrystalline indium. *J. Exp. Theor. Phys. Lett.* **2017**, *106*, 35–39. [CrossRef]
9. Safonova, E.V.; Konchakov, R.A.; Mitrofanov, Y.P.; Kobelev, N.P.; Vinogradov, A.Y.; Khonik, V.A. Contribution of interstitial defects and anharmonicity to the premelting increase in the heat capacity of single-crystal aluminum. *J. Exp. Theor. Phys. Lett.* **2016**, *103*, 765–768. [CrossRef]
10. Montanari, R.; Varone, A. Anelastic phenomena preceding the melting of pure metals and alloys. *Mater. Sci. Forum* **2016**, *879*, 66–71. [CrossRef]

11. Montanari, R.; Varone, A. Physical phenomena leading to melting of metals. *Mater. Sci. Forum* **2016**, *884*, 3–17. [CrossRef]
12. Nowick, A.S.; Berry, B.S. *Anelastic Relaxation in Crystalline Solids*, 1st ed.; Academic Press: New York, NY, USA; London, UK, 1972.
13. Brunelli, L.; Gondi, P.; Montanari, R.; Coppola, R. Internal strains after recovery of hardness in tempered martensitic steels for fusion reactors. *J. Nucl. Mater.* **1991**, *179–181*, 675–678. [CrossRef]
14. Capotorto, C.; Coppola, R.; Gondi, P.; Montanari, R.; Tata, M.E. Tempering structures and related ductile to brittle transition in MANET steel. *Fusion Technol.* **1992**, *1*, 1311–1315.
15. Gondi, P.; Montanari, R. On the Cr atom distribution in MANET1 steel. *Phys. Stat. Sol. (a)* **1992**, *131*, 465–480. [CrossRef]
16. Coppola, R.; Gondi, P.; Montanari, R. Effects of C-Cr elementary aggregates on the properties of the MANET steel. *J. Nucl. Mater.* **1993**, *206*, 360–362. [CrossRef]
17. Gondi, P.; Montanari, R. Q^{-1}-spectra connected with C under solute atom interaction. *J. Alloys Compd.* **1994**, *211–212*, 33–36. [CrossRef]
18. Gondi, P.; Montanari, R.; Sili, A.; Coppola, R. Solute Cr atom distribution and fracture behaviour of MANET steel. *J. Nucl. Mater.* **1994**, *212–215*, 564–568. [CrossRef]
19. Coppola, R.; Lukas, P.; Montanari, R.; Rustichelli, F.; Vrana, M. X-ray and neutron line broadening measurements in a martensitic steel for fusion technology. *Mater. Lett.* **1995**, *22*, 17–21. [CrossRef]
20. Brokmeier, H.G.; Coppola, R.; Montanari, R.; Rustichelli, F. Neutron diffraction study of the crystalline texture in a martensitic steel for fusion reactor technology. *Phisica B Condens. Matter* **1995**, *213–214*, 809–811. [CrossRef]
21. Albertini, G.; Ceretti, M.; Coppola, R.; Fiori, F.; Gondi, P.; Montanari, R. Small-angle neutron scattering study of C Cr elementary aggregates in a martensitic steel for fusion-reactor technology. *Phisica B Condens. Matter* **1995**, *213–214*, 812–814. [CrossRef]
22. Gondi, P.; Montanari, R.; Sili, A.; Tata, M.E. Effects of thermal treatments on the ductile to brittle transition of MANET steel. *J. Nucl. Mater.* **1996**, *233–237*, 248–252. [CrossRef]
23. Gondi, P.; Donato, A.; Montanari, R.; Sili, A. A miniaturized test method for the mechanical characterization of structural materials for fusion reactors. *J. Nucl. Mater.* **1996**, *233–237*, 1557–1560. [CrossRef]
24. Gupta, R.; Gondi, P.; Montanari, R.; Principi, G.; Tata, M.E. Internal friction and Mössbauer study of C-Cr associates in MANET steel. *J. Mater. Res.* **1997**, *12*, 296–299.
25. Gondi, P.; Montanari, R.; Tata, M.E. Distribution of C-Cr associates and mechanical stability of Cr martensitic steels. *J. Nucl. Mater.* **1998**, *258–263*, 1167–1172. [CrossRef]
26. Amadori, S.; Campari, E.G.; Fiorini, A.L.; Montanari, R.; Pasquini, L.; Savini, L.; Bonetti, E. Automated resonant vibrating-reed analyzer apparatus for a non-destructive characterization of materials for industrial applications. *Mater. Sci. Eng. A* **2006**, *442*, 543–546. [CrossRef]
27. Gondi, P.; Montanari, R.; Coppola, R. On the statistical distribution of Cr atoms in Fe-Cr alloys with high swelling resistance in NFR. *J. Nucl. Mater.* **1992**, *191–194*, 1274–1278. [CrossRef]
28. Blanter, M.S.; Golovin, I.S.; Neuhäuser, H.; Sinning, H.-R. *Internal Friction in Metallic Materials. A Handbook*; Springer: Berlin, Germany, 2007.
29. Tomilin, I.A.; Sarrak, V.I.; Gorokhova, N.A.; Suvorova, S.O.; Zhukov, L.L. Non-regular carbon atom distribution in iron-chromium alloys. *Phys. Met. Metallogr.* **1983**, *56*, 501–506.
30. Ritchie, I.G.; Rawlings, R. Snoek Peaks in Ternary Iron-Nitrogen Alloys. *Acta Metall.* **1967**, *15*, 491–496. [CrossRef]
31. Tiwari, G.P.; Bose, A.; Chakravartty, J.K.; Wadekar, S.L.; Totlani, M.K.; Arya, R.N.; Fotedar, R.K. A study of internal hydrogen embrittlement of steels. *Mater. Sci. Eng. A* **2000**, *286*, 269–281. [CrossRef]
32. Lu, Q.; Atrens, A. A critical review of the influence of hydrogen on the mechanical properties of medium-strength steels. *Corros. Rev.* **2013**, *31*, 85–103. [CrossRef]
33. Lynch, S.P. Hydrogen embrittlement (HE) phenomenon and mechanisms. In *Stress Corrosion Cracking: Theory and Practice*; Raja, V.S., Shoji, T., Eds.; Woodhead Publishing: Cambridge, UK, 2011; pp. 90–130.
34. Kumar, B.S.; Kain, V.; Singh, M.; Vishwanadh, V. Influence of hydrogen on mechanical properties and fracture of tempered 13 wt % Cr martensitic stainless steel. *Mater. Sci. Eng. A* **2017**, *700*, 140–151. [CrossRef]
35. Turnbull, A.; Carroll, M.W.; Ferriss, D.H. Analysis of hydrogen diffusion and trapping in a 13% chromium martensitic stainless steel. *Acta Metall.* **1989**, *31*, 2039–2046. [CrossRef]

36. Shewmon, P.G. Hydrogen attack of carbon steel. *Metall. Trans. A* **1976**, *7*, 279–286. [CrossRef]

37. Lacombe, P.; Aucouturier, M.; Chene, J. *Hydrogen Embrittlement and Stress Corrosion Cracking*; ASM: Metals Park, OH, USA, 1984; p. 79.

38. Coppola, R.; Gondi, P.; Montanari, R.; Veniali, F. Structure evolution during heat treatments of 12% Cr martensitic steel for NET. *J. Nucl. Mater.* **1988**, *155–157*, 616–619. [CrossRef]

39. *JCPDS-International Centre for Diffraction Data*; Version 2.14; Library of Congress: Newtown Square, PA, USA, 1987–1994.

40. Dyson, D.J.; Andrews, K.W. Carbide M_7C_3 and its formation in alloy steels. *J. Iron Steel Inst.* **1969**, *207*, 208–219.

41. Honeycombe, R.W.K. *Steels Microstructure and Properties*, 3rd ed.; Edward Arnold: London, UK, 1990; p. 158.